THESIS FOR THE DEGREE OF LICENTIATE OF ENGINEERING

Measurements and Validation of Integrated and Active Antenna Arrays

Iaroslav Shilinkov

Department of Electrical Engineering
Chalmers University of Technology
Gothenburg, Sweden, 2026

Measurements and Validation of Integrated and Active Antenna Arrays

Iaroslav Shilinkov

Department of Electrical Engineering
Chalmers University of Technology
SE-412 96 Gothenburg, Sweden
Phone: +46 (0)31 772 1000

Printed by Chalmers Digital Printing
Gothenburg, Sweden, May 2026

Abstract

Active integrated antennas (AIAs), including antenna-in-package (AiP) and antenna-on-chip (AoC) implementations, tightly couple radiating structures with active circuitry and therefore lack accessible antenna ports. While this integration improves efficiency, compactness, and beamforming capability at millimeter-wave and sub-terahertz frequencies, it fundamentally complicates measurement and validation. Traditional characterization methods are often infeasible due to the absence of accessible antenna ports, and conventional over-the-air (OTA) techniques primarily provide field-based observables such as radiation patterns and radiated power, offering limited direct insight into terminal electrical quantities.

This licentiate thesis addresses the challenge of extracting electrically meaningful information from integrated antenna arrays without direct RF access. A scalable backscattering-based OTA measurement framework is developed, in which controlled load modulation at the antenna ports enables reconstruction of input impedance and realized gain from remotely measured scattering responses. The methodology is extended from single-element demonstrations to array-level characterization and reconfigurable intelligent surfaces (RIS), establishing a generalized measurement architecture suitable for integrated apertures with embedded switching capabilities.

In parallel, electronically controlled load-pull techniques are investigated as a complementary tool for validating active RF devices under realistic antenna-imposed loading conditions. A compact, self-contained load-pull measurement platform is implemented to emulate dynamic load environments and study device behavior in integrated contexts.

Together, these contributions advance the measurement and validation of active integrated antenna systems by bridging field-based OTA observations and terminal-level electrical characterization, enabling more reliable system-level verification of highly integrated millimeter-wave architectures.

Keywords: Antenna measurements, backscattering, antenna arrays, load-pull.

List of Publications

This thesis is based on the following publications:

[A] **Iaroslav Shilinkov**, Rob Maaskant, "Antenna Array Measurements by a Scalable Backscatter Modulation Procedure". Published in IEEE AWPL, 2024.

[B] **Iaroslav Shilinkov**, Rob Maaskant, Gregor Lasser, "Open-loop Active Load-pull Setup Using the ZCU216 Radio Frequency System-on-Chip". Published in IEEE MWTL, 2025.

[C] **Iaroslav Shilinkov**, Viktor Chernikov, Rob Maaskant, Marianna Ivashina, "Antenna Characterization by the Back-Scattering Measurement Method Using the Integrated RF-Frontend as Load Modulation Device". Published at ICEAA 2024.

[D] **Iaroslav Shilinkov**, Oleg Iupikov, Pavlo Krasov, Yuqing Zhu, Rob Maaskant, Marianna Ivashina, "Measurement of Reconfigurable Intelligent Surfaces Through the Back-Scattering Method: Demonstration at 28 GHz". Published at EuCAP 2025.

Other publications by the author, not included in this thesis, are:

[E] J. Aronsson, H. Schreckenbach, **I. Shilinkov**, R. Maaskant, "BEM-Based Characterization of a D-Band On-Chip Patch Antenna Array". *2026 IEEE 76th Electronic Components and Technology Conference (ECTC)*, Orlando, Florida, May. 2026.

Contents

Acknowledgments

I would like to express my sincere gratitude to my supervisor, Prof. Rob Maaskant, for his guidance, insightful discussions, and continuous support throughout this work. His expertise has been invaluable for shaping the ideas presented in this thesis.

I am also deeply grateful to my co-supervisor, Dr. Gregor Lasser, for many helpful discussions and for his guidance on nonlinear devices and load-pull measurements, which significantly contributed to this research.

I would like to thank Prof. Marianna Ivashina for fostering a stimulating and supportive research environment at the Antenna Systems group at Chalmers University of Technology.

I would like to thank Viktor Chernikov, Oleg Iupikov, and Pavlo Krasov, as well as the rest of the Antenna Systems group, for many enjoyable and fruitful lunchtime discussions that often sparked new ideas and helped shape this work.

This work has been supported by several research initiatives. In particular, I would like to acknowledge the EUREKA EURIPIDES2 InnoStar project for financial support. I would also like to acknowledge funding from the Chalmers–Lund Center for Advanced Semiconductor System Design (ClassIC), which is funded by the Swedish Foundation for Strategic Research.

Finally, I would like to thank my family and friends for their continuous support and encouragement.

Acronyms

AIA:	Active Integrated Antenna
AiP:	Antenna-in-Package
AoC:	Antenna-on-Chip
OTA:	Over-the-Air
RIS:	Reconfigurable Intelligent Surface
UC:	Unit Cell
RF:	Radio Frequency
RFIC:	Radio-Frequency Integrated Circuit
RFSoC:	Radio Frequency System-on-Chip
PA:	Power Amplifier
LNA:	Low-Noise Amplifier
DUT:	Device Under Test
AUT:	Antenna Under Test
CA:	Chamber Antenna
VNA:	Vector Network Analyzer
LP:	Load-Pull
DDS:	Direct Digital Synthesis
DAC:	Digital-to-Analog Converter
ADC:	Analog-to-Digital Converter
EEP:	Embedded Element Pattern
EIRP:	Effective Isotropic Radiated Power
TRP:	Total Radiated Power

DFF:	Direct Far-Field
IFF:	Indirect Far-Field
NF:	Near-Field
FF:	Far-Field
RC:	Reverberation Chamber
PAE:	Power-Added Efficiency
PAPR:	Peak-to-Average Power Ratio
QAM:	Quadrature Amplitude Modulation
MIMO:	Multiple-Input Multiple-Output
PCB:	Printed Circuit Board
LTCC:	Low-Temperature Co-Fired Ceramic
ICT:	Information and Communication Technology
GHG:	Greenhouse Gas
BPF:	Band-Pass Filter

Part I

Overview

CHAPTER 1

Introduction

1.1 Motivation

The continuous growth in mobile data traffic and the demand for higher data rates have been a key driving force behind the evolution of modern wireless communication systems. To meet these demands within the limited available spectrum, increasingly spectrally efficient modulation schemes are employed, such as high-order quadrature amplitude modulation (QAM) in combination with wideband multi-carrier waveforms. A well-known consequence of such modulation formats is their inherently high peak-to-average power ratio (PAPR) [1].

High PAPR signals force radio-frequency (RF) power amplifiers (PAs) to operate with significant output power back-off in order to maintain linearity and satisfy spectral emission requirements. As a result, the power-added efficiency (PAE) of the PA is severely degraded, since most conventional PA architectures achieve their peak efficiency only near saturation [2]. This effect becomes increasingly critical in modern base stations and user equipment, where a large fraction of the total power consumption is associated with RF transmission.

In parallel, modern wireless systems rely heavily on multiple-input multiple-output (MIMO) and phased antenna arrays to increase spectral efficiency, coverage, and link reliability. While such architectures provide substantial performance gains, they also require a large number of parallel RF transceiver chains and power amplifiers. Consequently, inefficiencies at the level of individual RF components accumulate and translate directly into increased system-level energy consumption [3].

From a broader perspective, the information and communication technology (ICT) sector contributes a non-negligible share of global greenhouse gas (GHG) emissions. Recent studies estimate that ICT accounts for several percent of global electricity consumption, with wireless access networks representing a significant and rapidly growing portion due to both infrastructure operation and device manufacturing [4], [5]. Although successive generations of mobile communication systems (from 2G and 3G to 4G and 5G) have improved energy efficiency per transmitted bit, the overall energy footprint continues to grow due to the increasing traffic demand [4].

These concerns are reflected in regulatory and policy frameworks, such as the European Climate Law, which establishes legally binding targets for climate neutrality and places increasing emphasis on energy-efficient technologies across all sectors, including telecommunications [6]. In this context, further reductions in the energy consumption of wireless networks are of both economic and societal importance.

To continue improving the efficiency of wireless systems, it is no longer sufficient to optimize individual RF building blocks in isolation. Instead, a system-level perspective is required, in which traditionally separate parts of the RF chain are co-designed and tightly integrated [7]. One prominent example is the integration of power amplifiers directly with antennas or antenna arrays, forming so-called active integrated antennas. By integrating matching networks directly into the antenna, such architectures reduce losses and total device size while offering the potential for substantially improved overall efficiency

At the same time, this high degree of integration introduces significant challenges. In active integrated antenna systems, the antenna and active circuitry are no longer independent entities, and classical concepts such as well-defined antenna ports or standardized reference impedances may no longer exist. As a consequence, conventional measurement and characterization techniques be-

come difficult or even inapplicable. In particular, validating the performance of active integrated antennas and integrated antenna arrays, where direct access to the antenna port is unavailable, requires alternative measurement approaches capable of operating at the system level.

Motivated by these challenges and opportunities, this thesis focuses on the measurement and characterization of active integrated antennas and antenna arrays. The goal is to develop and evaluate measurement methodologies that accurately capture the performance of tightly integrated antenna and antenna array systems, thereby enabling the design and optimization of energy-efficient wireless communication technologies.

1.2 Active Integrated Antennas

Active integrated antennas (AIAs) are systems in which radiating elements are co-designed and co-integrated with active circuitry such as power amplifiers (PAs), low-noise amplifiers (LNAs), switches, phase shifters, oscillators, or complete transceiver front-ends. In contrast to conventional RF architectures with standardized 50 Ω interfaces and clearly defined reference planes, in AIAs the antenna is a part of the active device's load environment and can be used as a functional element in the device's matching. Intermediate interconnects, transitions, and external matching networks are often intentionally eliminated in order to reduce insertion loss, footprint, and cost [7], [8].

Active integrated antennas span a wide range of technologies and integration levels. Packaging-wise they can be realized at the board level, package level, or directly on chip, and frequently combine multiple integration domains in hybrid solutions.

Board-level and module-level integration. In board-level implementations, antennas and active electronics are realized on a common printed circuit board (PCB) or multi-layer module substrate, typically with packaged integrated circuits mounted in close proximity to the radiating elements. This approach remains attractive for prototyping and for lower mmWave bands, and is widely used in practical phased-array demonstrators and cost-oriented 28 GHz array modules [11], [12]. Although short RF traces may still exist between device and radiator, the antenna impedance already strongly influences the active device operation.

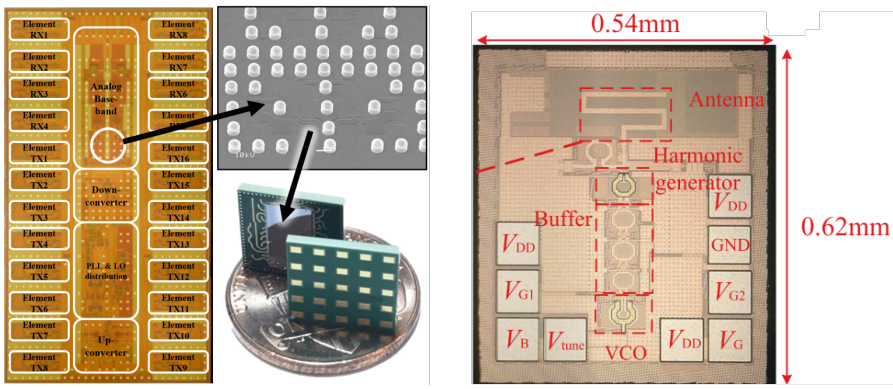

(a) Antenna-in-package (AiP) photo [9].

(b) Antenna-on-chip (AoC) from [10].

Figure 1.1: Schematic categorization of active integrated antennas based on packaging technology.

Antenna-in-package (AiP). In antenna-in-package solutions, the antenna array and one or multiple RFICs are integrated within the same package using technologies such as LTCC, or organic substrates. AiP is widely adopted for highly integrated mmWave beamforming modules, because it combines compactness with reduced RF loss and scalable array assembly [12]–[18]. In many realizations, the antenna structure forms part of the output or input matching network of the active device.

Antenna-on-chip (AoC). At very high frequencies, antennas can be integrated directly on silicon or within the chip stack. Such antenna-on-chip implementations enable extreme miniaturization and wafer-level scalability, but efficiency is often limited by substrate losses and metallization constraints [19], [20].

This division is not strict, and there are many examples of hybrid approaches, but it serves to illustrate the diversity of integration strategies and the corresponding implications for design and measurement.

Regardless of the packaging technology, active integrated antennas can also be categorized based on the active device co-integrated with the antenna.

From a system perspective, AIAs can also differ in the integrated active function. Transmit arrays integrate PAs with radiators and may exploit direct

matching or harmonic shaping through the antenna geometry [8], [21], [22]. Receive architectures integrate LNAs with antennas for joint impedance and noise optimization [23], [24]. Highly integrated transceiver arrays combine beamforming ICs and radiators into compact steerable apertures [12], [15], [18]. In oscillator-based architectures, frequency generation and radiation are merged into a single structure [25].

Despite their diversity, active integrated antennas share a fundamental characteristic: the absence of a well-defined, physically accessible antenna port. In many implementations, there is no standardized 50 Ω reference plane at the antenna interface, and the antenna impedance forms part of the matching environment of the active device. The effective load presented to the device is therefore determined not only by local matching structures, but also by array coupling, bias conditions, beamforming configuration, and the surrounding environment.

As a consequence, conventional S-parameter measurements, which rely on physically accessible ports and well-defined reference impedances, cannot be directly applied at the antenna interface. At the same time, over-the-air measurements alone do not provide direct access to the electrical quantities at the device terminals.

In this thesis, the characterization problem is addressed by separating the analysis of the active device from that of the antenna structure. First, the active device is characterized under large-signal conditions so that its behavior is known for a range of load impedances. Second, the integrated antenna or antenna array is characterized using over-the-air (OTA) measurement techniques that do not require direct electrical access to the antenna ports. Combining these two aspects enables validation of active integrated antenna systems even when a conventional antenna port is not available.

1.3 Measurement techniques for integrated RF systems

This section provides an overview of the two principal measurement domains that form the methodological foundation of this thesis.

Second, over-the-air (OTA) measurement techniques are discussed as the primary framework for characterizing integrated antennas and arrays in the absence of direct port access.

Together, large-signal device characterization and OTA antenna characterization define the measurement space within which the contributions of this thesis are positioned.

Large signal measurements of active RF devices

Large-signal characterization of active RF devices requires controlled variation of the impedance presented at the device ports. Load-pull (LP) measurements address this need by synthesizing different source and/or load reflection coefficients while recording performance metrics such as output power, efficiency, gain compression, and linearity [26]–[28]. Over the years, numerous load-pull implementations have been proposed. Rather than classifying them by application domain (harmonic, wideband, modulated, etc.), it is more instructive to distinguish them by their impedance synthesis architecture.

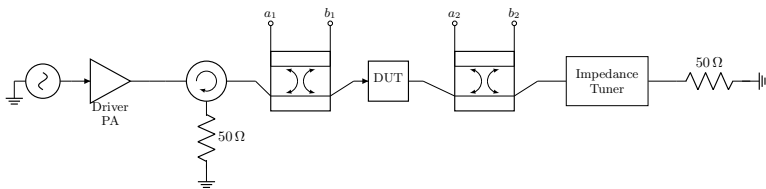

Figure 1.2: Schematic of an example passive load-pull measurement system.

Passive load-pull systems

Passive load-pull employs mechanically tunable impedance networks, typically based on slide-screw or slug tuners, to present a desired reflection coefficient at the fundamental frequency. These systems are robust, offer high power handling capability, and remain widely used for baseline device characterization and modeling [27]. However, passive approaches suffer from several limitations: (i) restricted Smith chart coverage due to insertion loss, (ii) slow mechanical tuning, (iii) narrowband operation, and (iv) limited control over harmonic impedances. Since the work presented in this thesis focuses on electronically reconfigurable impedance environments and dynamic loading effects, passive tuner-based systems are outside its scope.

Active load-pull systems

In active load-pull systems, the desired reflection coefficient is synthesized by electronically injecting a controlled signal wave at the DUT output. This approach overcomes the loss limitations of passive tuners and enables rapid, programmable impedance control [26], [29]. Because the impedance is synthesized with the secondary source, active systems can, in principle, reach any point on the Smith chart, including regions not accessible with passive hardware.

Active load-pull systems are commonly implemented in either closed-loop or open-loop configurations.

In closed-loop systems, the DUT output signal is sampled, amplified, phase-shifted, and re-injected to synthesize the desired load condition. Such architectures enable high reflection coefficient magnitudes and multi-harmonic control with only one RF input signal, but they require careful stabilization and calibration [30], [31].

In open-loop systems, the injected wave is generated independently of the DUT output and programmed directly, typically using signal generators or arbitrary waveform generators. Open-loop architectures are often more stable and simpler to calibrate, compared to closed-loop setups. [32], [33].

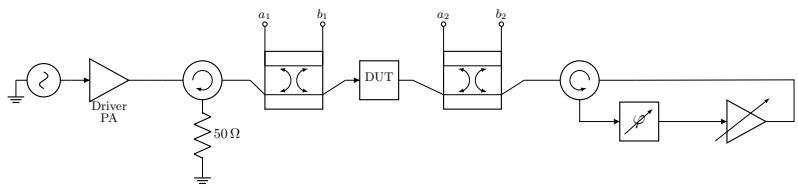

(a) Closed-loop active load-pull

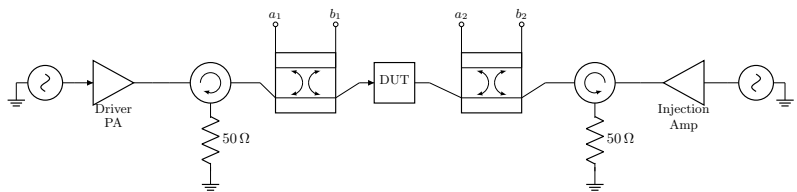

(b) Open-loop active load-pull

Figure 1.3: Conceptual comparison of closed-loop and open-loop active load-pull architectures.

Precise control of the synthesized load in both types of active LP setups makes large-signal characterization of the active device possible at multiple harmonics [34], and with modulated signals [32], and it can allow for time domain control of the RF load-line of the DUT [35].

Relevance to integrated RF systems

For integrated and array-based transmitters, the effective load presented to each active device may vary dynamically due to antenna coupling, beam steering, and environmental interactions. Active load-pull systems, particularly electronically controlled open-loop implementations, therefore provide a natural experimental framework for emulating and studying such dynamic loading conditions [36], [37]. This architectural perspective on load-pull serves as a bridge toward the integrated and over-the-air load modulation concepts developed in the following sections.

OTA measurements of integrated antennas and arrays.

The measurement of integrated antennas and antenna arrays presents unique challenges compared to the characterization of standalone radiating elements. In antenna-in-package (AiP) and antenna-on-chip (AoC) implementations, direct electrical access to antenna ports is often unavailable, precluding conventional VNA-based impedance and S-parameter measurements [38]. Furthermore, probe-station measurements might be problematic because the RF probe is located in the radiating near-field of the DUT and may be electrically large at millimeter-wave and sub-THz frequencies, thereby perturbing the antenna radiation behavior. As a result, characterization must rely primarily on the radiated quantities obtained through over-the-air (OTA) techniques.

OTA characterization

Standard OTA strategies include direct far-field (DFF), indirect far-field (IFF), near-field (NF) scanning, and midfield approaches [38]. These methods differ in measurement geometry and post-processing requirements but share a common principle: they measure the radiated electromagnetic field.

In direct far-field measurements, the complex far-field distribution is sampled and used to derive radiation patterns, gain, effective isotropic radiated

power (EIRP), and total radiated power (TRP) [39]. For integrated antennas, however, the lack of RF port access imposes fundamental constraints. The device under test (DUT) must either operate as an active transmitter or incorporate on-chip detection circuitry in receive mode. In transmit mode, only radiated field metrics are directly observable; input impedance and reflection coefficients are not accessible. In receive mode, the detected output depends jointly on antenna impedance, matching network, and receiver circuitry. Consequently, impedance matching and embedded element behavior must be inferred indirectly.

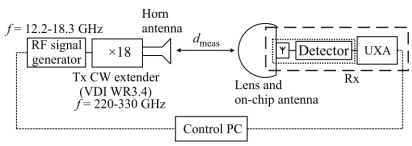

(a) Schematic illustration of far-field OTA measurement [39].

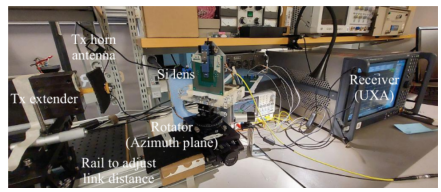

(b) Photograph of the experimental far-field setup [39].

Figure 1.4: Example far-field OTA characterization of an integrated antenna.

To reduce spatial requirements and enable compact measurement setups, near-field and midfield approaches have been proposed. By sampling the complex electromagnetic field in the radiating near-field of the DUT and applying NF–FF reconstruction algorithms, far-field quantities can be obtained without requiring full Fraunhofer distances [40]. Such approaches have been experimentally demonstrated for AiP phased arrays using multi-axis planar scanners, enabling OTA calibration and radiation pattern reconstruction within a compact environment [41].

Reverberation chamber (RC) techniques represent another extension of OTA characterization. By generating statistically uniform and isotropic fields, RC-based methods enable the extraction of total radiated power, efficiency, and diversity-related metrics without strict far-field conditions. More recently, RC techniques have been extended beyond radiation metrics to enable over-the-air noise figure and system gain measurements of active integrated antennas using controlled hot and cold noise environments inside the chamber [42].

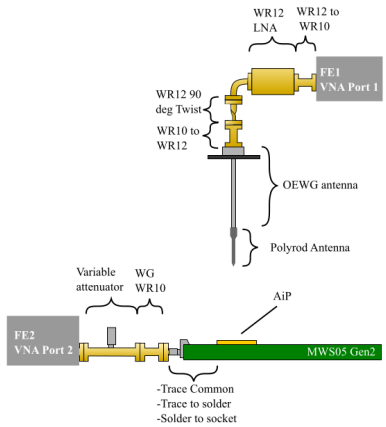

Figure 1.5: Hybrid near-field/far-field OTA measurement setup for a W-band AiP phased array, employing a multi-axis scanner and phase-coherent measurements. Adapted from [41].

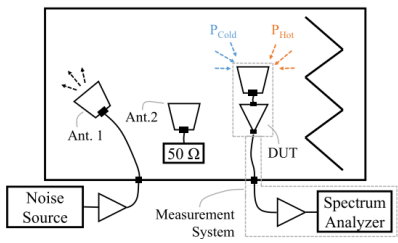

Figure 1.6: Conceptual illustration of OTA noise-figure measurement using a reverberation chamber [42].

These results demonstrate that OTA methods can be used to recover certain receiver-level performance parameters in the absence of direct RF access.

Backscattering-based impedance reconstruction

A fundamentally different class of OTA techniques is based on controlled backscattering modulation. Instead of observing only the radiated field, these methods intentionally vary the antenna port termination and analyze the resulting change in the reradiated field. By illuminating the antenna under test (AUT) with a reference antenna and electronically switching the AUT load between multiple impedance states, the reflection measured at the reference antenna can be used to reconstruct the AUT input impedance and realized gain through a multi-state scattering formulation [43].

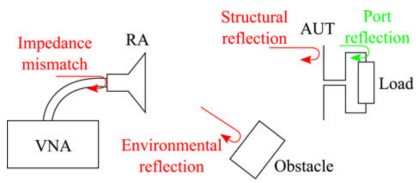

Figure 1.7: Schematic of the backscattering measurement setup from [44].

This approach has recently been demonstrated for a D-band on-chip antenna monolithically integrated with a reflective load switch, enabling contactless impedance reconstruction without RF probe access [45]. Unlike other measurement approaches discussed previously, backscattering methods do allow for passive S-parameters extraction of the passive part of AiAs.

Measurement limitations and open challenges

Conventional OTA techniques, whether based on far-field, near-field, or reverberation chamber environments, primarily provide field-based observables. While these methods accurately characterize radiated performance, they offer limited direct access to terminal electrical quantities such as input impedance, embedded element loading, or mutual coupling.

Backscattering-based approaches demonstrate that electrically meaningful antenna parameters can be reconstructed over the air through controlled load

modulation. Existing demonstrations have validated this principle at the single-element level, yet its extension to scalable array-level characterization and practical measurement architectures has remained largely unexplored.

The development of a generalized and scalable backscattering-based framework for integrated antenna arrays constitutes a central contribution of this thesis.

1.4 Contributions of this thesis

The main contributions of this licentiate thesis are centered on the measurement and validation of integrated antenna arrays from a system-level perspective. In particular, the thesis makes the following contributions:

- Development of a scalable backscattering-based over-the-air measurement framework for antenna arrays without direct electrical access to antenna ports, but with integrated switchable loads (**Papers A, C**).
- Application of the backscattering measurement method to integrated antenna arrays and RIS (**Paper D**).
- Investigation of load-pull techniques as a means of validating active RF devices under realistic antenna-imposed load conditions and hardware implementation of low-cost self-contained measurement setup based on the ZCU216 RFSoC board (**Paper B**).

1.5 Structure of this thesis

This licentiate thesis consists of two parts. Part I provides a summary of the research topic and the main contributions, while Part II contains the appended publications.

Chapter 1 introduces active integrated antennas and discusses the measurement challenges that arise when antenna ports are inaccessible and when the antenna is tightly integrated with active circuitry. Existing over-the-air and load-modulation-based approaches are briefly reviewed.

Chapter 2 presents a backscattering-based over-the-air method for reconstructing the passive S-parameters of integrated antenna arrays. A matrix

formulation for the multiport problem is introduced together with a systematic extraction procedure. Particular attention is given to phase-sign ambiguity and impedance renormalization. The method is validated numerically and illustrated on a 28 GHz reconfigurable intelligent surface unit cell with tunable components.

Chapter 3 describes a compact open-loop active load-pull measurement setup implemented on a single RFSoC evaluation board. The system architecture, calibration strategy, and impedance synthesis model are presented. The setup is validated through return-loss, small-signal gain, and load-pull measurements of a commercial RF power amplifier.

Chapter 4 summarizes the appended papers and clarifies their individual contributions.

Chapter 5 concludes the thesis and outlines possible directions for further research.

CHAPTER 2

Backscattering OTA Measurements of Integrated Antenna Arrays

This chapter presents a backscattering over-the-air measurement technique for integrated antenna arrays. The method enables the extraction of the passive scattering parameters and embedded element patterns (EEP) of the array without direct access to the antenna ports by modulating loads present to the array elements. Phase ambiguity is discussed and resolved in the monostatic case by relying on the geometry of the array and the finite probe distance. This method is validated through numerical simulations, and also usage of RF front-end as tunable loads is also speculated. Also, this method was applied to a 27-GHz RIS unitcell when pin-diodes and varactors are embedded directly in the aperture.

Problem formulation

Consider an integrated antenna array consisting of N antenna ports, illuminated by a chamber antenna connected to a one-port VNA. Due to the absence of direct electrical access to the antenna ports, the passive electromagnetic behavior of the array must be evaluated indirectly through over-the-air inter-

action.

The combined measurement setup is modeled as a passive, linear, time-invariant $(N+1)$-port network. Port 1 corresponds to the probe antenna, while ports 2 through $N+1$ correspond to the antenna array ports. The scattering behavior of the combined system is described by the scattering matrix

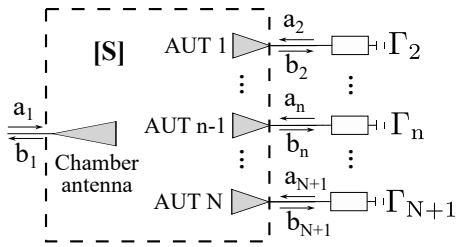

Figure 2.1: Schematic of the backscattering measurement setup for an antenna array.

$$\begin{bmatrix} b_1 \\ \mathbf{b} \end{bmatrix} = \mathbf{S} \begin{bmatrix} a_1 \\ \mathbf{a} \end{bmatrix} \tag{2.1}$$

where $\mathbf{a}$ and $\mathbf{b}$ are the vectors of the forward and backward wave amplitudes at the AUT ports, respectively. Furthermore,

$$\mathbf{S} = \begin{bmatrix} S_{11} & \mathbf{S}_{\mathrm{CA,AUT}} \\ \mathbf{S}_{\mathrm{AUT,CA}} & \mathbf{S}_{\mathrm{AUT}} \end{bmatrix} \tag{2.2}$$

where S_{11} is the CA port reflection coefficient if $\mathbf{a} = \mathbf{0}$, $\mathbf{S}_{\mathrm{AUT,CA}}$ and $\mathbf{S}_{\mathrm{CA,AUT}}$ are $N \times 1$ and $1 \times N$ vectors composed of transmission coefficients from the chamber antenna to AUT and from AUT to chamber antenna, respectively, and $\mathbf{S}_{\mathrm{AUT}}$ is the $N \times N$ scattering matrix composed of reflection coefficients of the AUT array elements and coupling coefficients between them.

The antenna array ports are terminated with known, controllable reflection coefficients collected in the diagonal matrix

$$\mathbf{\Gamma} = \mathrm{diag}(\Gamma_2, \Gamma_3, \ldots, \Gamma_{N+1}). \tag{2.3}$$

so one can write $\mathbf{a} = \mathbf{\Gamma b}$. The goal is to extract the scattering matrix $\mathbf{S}_{\mathrm{AUT}}$ of the antenna array from measurements of the backscattered signal at the probe antenna, which corresponds to b_1 in (2.1).

It is well known that the scattering parameters for partially terminated multiport networks can be calculated as follows:

$$\widehat{S}_{11} = S_{11} + \mathbf{S}_{\mathrm{AUT,CA}}^{\mathsf{T}} \left(\mathbf{I} - \mathbf{\Gamma}\mathbf{S}_{\mathrm{AUT}}\right)^{-1} \mathbf{\Gamma}\mathbf{S}_{\mathrm{AUT,CA}} \tag{2.4}$$

Equation (2.4) forms the basis of the proposed measurement approach. The unknown quantity of interest is the antenna array scattering matrix $\mathbf{S}_{\mathrm{AUT}}$ as well as $\mathbf{S}_{\mathrm{AUT,CA}}$ – transmission coefficients between CA and AUT, while $\widehat{S}_{11}$ is directly measurable for different realizations of $\mathbf{\Gamma}$.

This equation is, in general, nonlinear in $\mathbf{S}_{\mathrm{AUT}}$ due to the matrix inverse. However, by carefully designing the load modulation strategy (i.e., selecting specific $\mathbf{\Gamma}$ configurations), it is possible to isolate the contributions of individual scattering parameters and recover $\mathbf{S}_{\mathrm{AUT}}$ in a systematic manner.

2.1 Measurement procedure

The procedure to extract the scattering parameters of the antenna array involves three main steps: measuring the reflection coefficient of the probe antenna when all AUT ports are terminated with a matched load, then extracting the diagonal terms of $\mathbf{S}_{\mathrm{AUT}}$ by modulating one port at a time, and finally recovering the mutual coupling terms by jointly modulating pairs of ports.

Step 1 The first step is to measure the reflection coefficient $\widehat{S}_{11}^{(0)}$ at the probe antenna when all AUT ports are terminated with a matched load, i.e., $\Gamma_n = 0$ for all n. This provides a baseline measurement that captures the direct reflection from the probe and structural scattering. The resulting expression simplifies to

$$\widehat{S}_{11}^{(0)} = S_{11} \tag{2.5}$$

Step 2 Next, to extract the S_{nn} and S_{n1}^2 elements of $\mathbf{S}_{\mathrm{AUT}}$, each port n is individually modulated while all other ports remain terminated with the matched load. Specifically, port n is switched between k distinct load states while $\Gamma_m = 0$ for all $m \neq n$. It can be shown that this case is the same as for two-port network, so the measured reflection coefficient at the probe antenna can be expressed as

$$\widehat{S}_{11} = S_{11} + \frac{S_{n1}^2 \Gamma_n}{1 - \Gamma_n S_{nn}} \quad \text{where } \Gamma_m = 0 \text{ for } m \neq n \tag{2.6}$$

where $n \in \{2, 3, \ldots, N+1\}$ and $m = 2, 3, \ldots, N+1$. For measurements $k = 1, \ldots, K$ this leads to the matrix equation

$$\begin{bmatrix} \widehat{S}_{11}^{(1)} \\ \widehat{S}_{11}^{(2)} \\ \vdots \\ \widehat{S}_{11}^{(K)} \end{bmatrix} = \begin{bmatrix} 1 & \widehat{S}_{11}^{(1)}\Gamma_n^{(1)} & \Gamma_n^{(1)} \\ 1 & \widehat{S}_{11}^{(2)}\Gamma_n^{(2)} & \Gamma_n^{(2)} \\ \vdots & \vdots & \vdots \\ 1 & \widehat{S}_{11}^{(K)}\Gamma_n^{(K)} & \Gamma_n^{(K)} \end{bmatrix} \begin{bmatrix} S_{11} \\ S_{nn} \\ S_{n1}^2 - S_{11}S_{nn} \end{bmatrix} \tag{2.7}$$

which can be solved for S_{11}, S_{nn}, and S_{n1}^2, if $K \geq 3$ [45], i.e., if one uses at least three different loads $\Gamma_n^{(k)}$, or at least two if S_{11} is known.

Step 3 In the final step, the mutual coupling terms S_{nm} with $m \neq n$ are recovered by jointly modulating a pair of ports while all remaining ports are terminated with the matched load. Specifically, ports n and m are assigned nonzero reflection coefficients Γ_n and Γ_m, while $\Gamma_\ell = 0$ for all $\ell \notin \{n, m\}$.

Under this condition, the matrix $\mathbf{\Gamma S}_{\mathrm{AUT}}$ contains only two nonzero rows corresponding to ports n and m. Consequently, the matrix

$$\mathbf{I} - \mathbf{\Gamma S}_{\mathrm{AUT}}$$

differs from the identity only in these two rows. By iterative application of the Laplace expansion, its determinant reduces to that of the corresponding 2×2 submatrix, i.e.,

$$\det(\mathbf{I} - \mathbf{\Gamma S}_{\mathrm{AUT}}) = \det \begin{bmatrix} 1 - \Gamma_n S_{nn} & -\Gamma_n S_{nm} \\ -\Gamma_m S_{mn} & 1 - \Gamma_m S_{mm} \end{bmatrix}. \tag{2.8}$$

To evaluate the inverse

$$(\mathbf{I} - \mathbf{\Gamma S}_{\mathrm{AUT}})^{-1},$$

the adjugate matrix must be computed. Due to the structure of $\mathbf{\Gamma}$, only the nth and mth rows of the cofactor matrix contribute after multiplication by $\mathbf{\Gamma}$. Moreover, it can be shown that the cofactor elements satisfy

$$C_{ij} = 0 \quad \text{for} \quad i \in \{n, m\},\ j \notin \{n, m\},$$

such that the product

$$(\mathbf{I} - \mathbf{\Gamma S}_{\mathrm{AUT}})^{-1}\mathbf{\Gamma}$$

contains only four nonzero entries.

Assuming reciprocity of the antenna array, i.e., $\mathbf{S}_{\mathrm{AUT}}$ is symmetric, and defining

$$X = \widehat{S}_{11} - S_{11},$$

Eq. (2.4) simplifies to

$$X = \frac{\begin{bmatrix} S_{n1} \\ S_{m1} \end{bmatrix}^{\mathsf{T}} \begin{bmatrix} \Gamma_n - \Gamma_n\Gamma_m S_{mm} & \Gamma_n\Gamma_m S_{nm} \\ \Gamma_n\Gamma_m S_{nm} & \Gamma_m - \Gamma_m\Gamma_n S_{nn} \end{bmatrix} \begin{bmatrix} S_{n1} \\ S_{m1} \end{bmatrix}}{(1-\Gamma_n S_{nn})(1-\Gamma_m S_{mm}) - \Gamma_n\Gamma_m S_{nm}^2}. \tag{2.9}$$

After completion of Steps 1 and 2, the quantities S_{11}, S_{nn}, S_{mm}, S_{n1}, and S_{m1} are already known. Therefore, Eq. (2.9) contains a single unknown parameter, S_{nm}, and reduces to a quadratic equation of the form

$$c_1 S_{nm}^2 + c_2 S_{nm} + c_3 = 0, \tag{2.10}$$

where

$$c_1 = X\Gamma_n\Gamma_m, \quad c_2 = 2\Gamma_n\Gamma_m S_{n1}S_{m1},$$

$$c_3 = \Gamma_n S_{n1}^2 + \Gamma_m S_{m1}^2 - \Gamma_n\Gamma_m\left(S_{n1}^2 S_{mm} + S_{m1}^2 S_{nn}\right) - X(1-\Gamma_n S_{nn})(1-\Gamma_m S_{mm}).$$

Since the coefficients c_i are complex-valued, two independent measurements with distinct load pairs (Γ_n, Γ_m) are sufficient to uniquely determine S_{nm}.

Phase-Sign Ambiguity In Step 2, the quantity S_{n1}^2 is recovered, implying that S_{n1} is determined only up to a sign. Both S_{n1} and $-S_{n1}$ satisfy the solution, introducing a phase-sign ambiguity.

This ambiguity propagates to the mutual coupling coefficients S_{nm} obtained in Step 3, since the coefficient c_2 in (2.10) depends linearly on $S_{n1}S_{m1}$. A sign change in either term alters the phase of S_{nm}.

While irrelevant for a single antenna, consistent phase relationships are essential for arrays, particularly for active reflection coefficient evaluation and beamforming based on embedded element patterns.

To resolve the ambiguity, a physical consistency constraint is imposed. It is assumed that phase variation between adjacent elements of $\mathbf{S}_{\mathrm{CA,AUT}}$ is minimal, which is justified for sufficiently large probe distances. After computing all possible sign combinations, the configuration minimizing phase discontinuities across neighboring terms is selected, yielding a globally consistent scattering matrix.

Impedance Renormalization Perfectly matched 50 Ω terminations are rarely available in practice. Therefore, the extraction procedure must account for arbitrary reference impedances.

Using Kurokawa's power-wave formulation [46], a change of reference impedance from Z_{old} to Z_{new} transforms the scattering matrix as

$$\mathbf{S}' = \mathbf{A}^{-1} \left(\mathbf{S} - \mathbf{\Gamma}^{\dagger} \right) \left(\mathbf{I} - \mathbf{\Gamma}\mathbf{S} \right)^{-1} \mathbf{A}^{\dagger}, \tag{2.11}$$

where $\mathbf{\Gamma} = \operatorname{diag}(r_i)$ contains the reflection coefficients of Z_{new} relative to Z_{old}, and $\mathbf{A}$ is defined accordingly.

In the power-wave formalism, zero reflections at an interconnection require conjugate-matched impedances. Consequently, load S-parameters are renormalized to Z_{new}^{*}, while the measured $\widehat{S}_{11}$ is referenced to Z_{new}.

This ensures impedance consistency of all quantities entering the extraction algorithm.

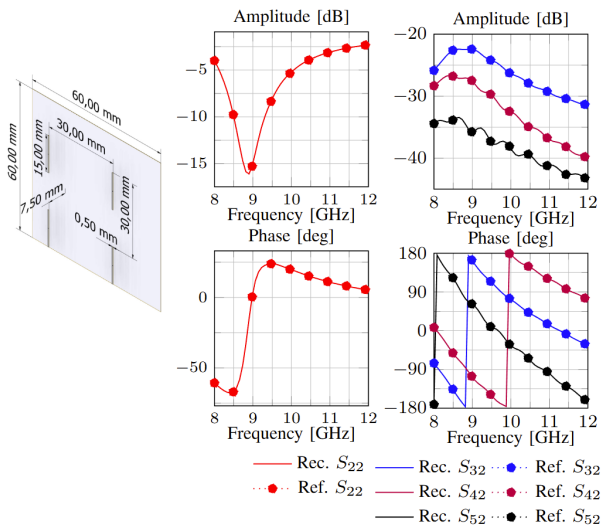

Figure 2.2: Simulated 2 × 2 dipole array.

This approach was tested in simulations for a 2 × 2 and 2 × 4 dipole array (Fig. 2.2), with a chamber antenna of identical dimensions and polarization (not shown) from a 240 mm distance and with a 6 mm vertical and horizontal

offset from the AUT's ground plane center. The AUT was terminated with loads from Fig. 2.4, and the probe reflection coefficient $\widehat{S}_{11}$ was computed for each load configuration.

As can be seen from Figs. 2.2 and 2.3, the S-parameters recovered with this method agree with the reference results within numerical precision.

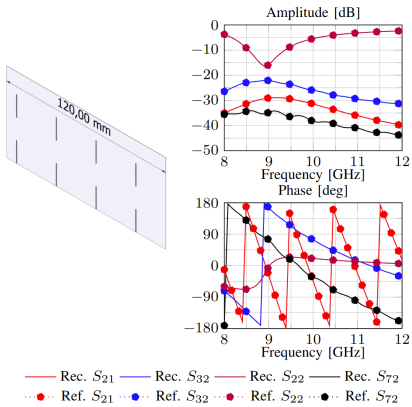

Figure 2.3: Simulated 2×4 dipole array.

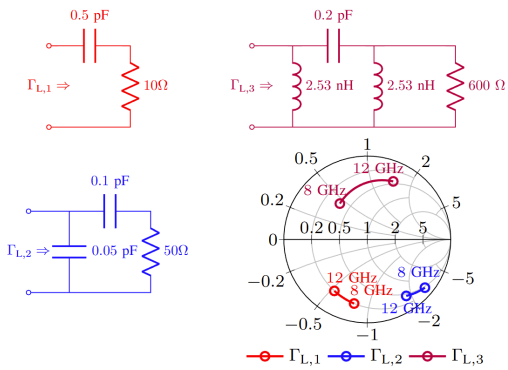

Figure 2.4: Load configurations used for scattering parameter extraction.

The terminations used for antenna characterization do not necessarily have to be dedicated, specially designed RF loads. Instead, the required set of

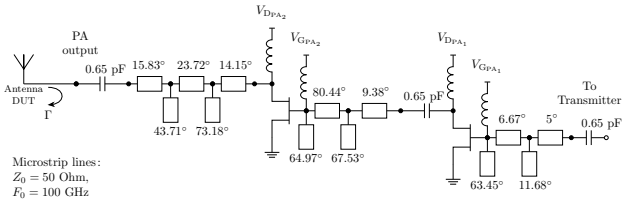

Figure 2.5: Schematic of the PA used for simulations in Paper C.

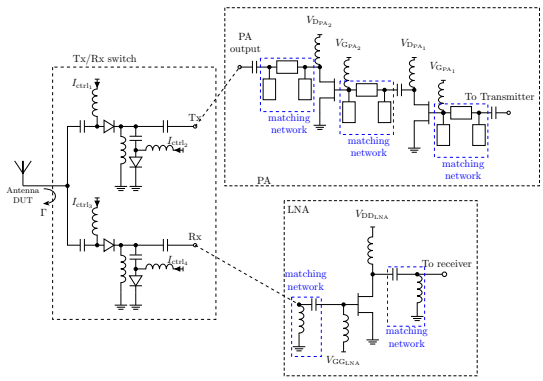

Figure 2.6: Schematic of the Tx/Rx switch used for simulations in Paper C.

distinct reflection states can be provided by the already integrated RF front-end connected to the antenna, which then acts as a load-modulation device. This avoids additional load-switching circuitry and leverages existing bias and control infrastructure.

Two representative cases were analyzed in Paper C. First, a Tx-only configuration was considered where the PA output is directly connected to the antenna (Fig. 2.5). Here, different load states are obtained by changing the PA bias conditions. Since at least three distinct loads are required for the basic inversion when S_{11} is not assumed known, the PA was operated in three bias states ("On", "Mid", "Off"), selected such that the resulting output reflection coefficients are sufficiently separated over frequency (Table I in Paper C and Fig. 2.7a).

Second, a half-duplex Tx/Rx front-end was analyzed (Fig. 2.6), where both the PA and LNA are deactivated and the reflection state is synthesized by the

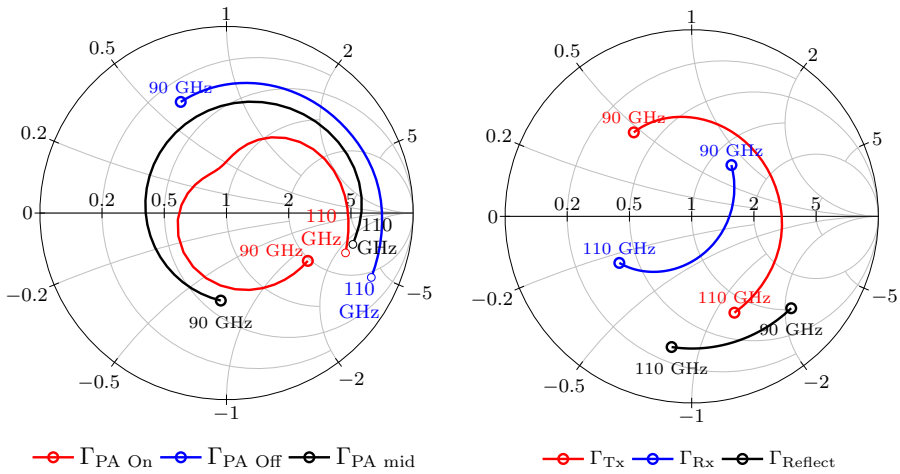

(a) Reflection coefficients synthesized by the PA under different biases.

(b) Reflection coefficients synthesized by the Tx/Rx switch in different modes.

Figure 2.7: Reflection states used for load modulation in the two frontend configurations considered in Paper C.

Tx/Rx switch alone. In this case, three switch modes ("Tx", "Rx", "Reflect") provide the necessary diversity in Γ (Table II in Paper C and Fig. 2.7b).

In both configurations, the simulated backscattering measurements confirm that using front-end state changes as the load-modulation mechanism is sufficient for accurate recovery of the passive DUT parameters, provided that the chosen states yield repeatable and well-separated reflection coefficients.

Element Pattern Recovery and Array Beamforming Beyond extracting the passive scattering matrix, the proposed backscattering framework enables recovery of embedded element patterns and full array radiation patterns once the multiport model of the AUT is reconstructed.

If either the chamber antenna (CA) or the AUT is mechanically rotated, element patterns can be recovered at each angular position. The recovery relies on the Friis transmission equation,

$$|S_{21}|^2 = G_{\Pi} \left(\frac{\lambda_0}{4\pi R} \right)^2, \tag{2.12}$$

where R is the phase-center distance and G_Π the gain product in the considered direction. Since the effective distance differs from the physical separation d, we write $R = d + \Delta d$, which leads to

$$\left(\frac{\lambda_0}{4\pi|S_{21}|}\right)^2 = \frac{1}{G_\Pi}(d + \Delta d)^2, \tag{2.13}$$

a quadratic expression in G_Π and Δd. Sweeping d and applying quadratic regression allows simultaneous estimation of both parameters.

By repeating this procedure over the desired angular range, the embedded element patterns are reconstructed.

Figure 2.8 shows representative recovered patterns for a 2×2 array, demonstrating excellent agreement with reference simulations except near deep nulls. The relative error,

$$\frac{|\mathbf{G}_{\text{ref}} - \widehat{\mathbf{G}}|}{\max(|\mathbf{G}_{\text{ref}}|)} \times 100\%, \tag{2.14}$$

remains below 0.5% for co-polar components.

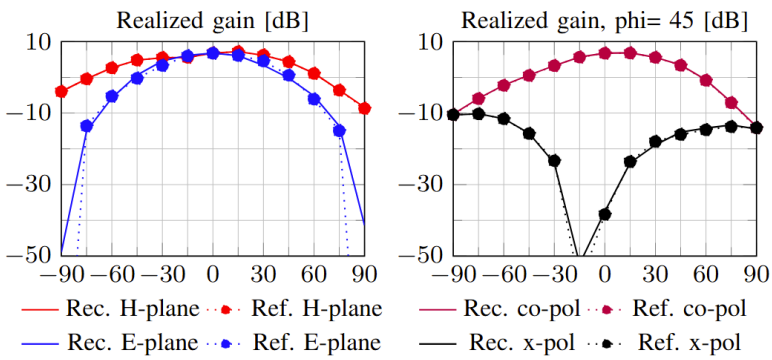

Figure 2.8: Recovered embedded element patterns.

Once the embedded patterns are known, the full array radiation pattern for arbitrary excitation vector $\mathbf{a}$ is obtained by setting $a_1 = 0$ in (2.1) and evaluating the normalized radiated power $\frac{|b_1|^2}{\mathbf{a}^\dagger \mathbf{a}}$.

Quadratic regression based on (2.13) yields the corresponding gain.

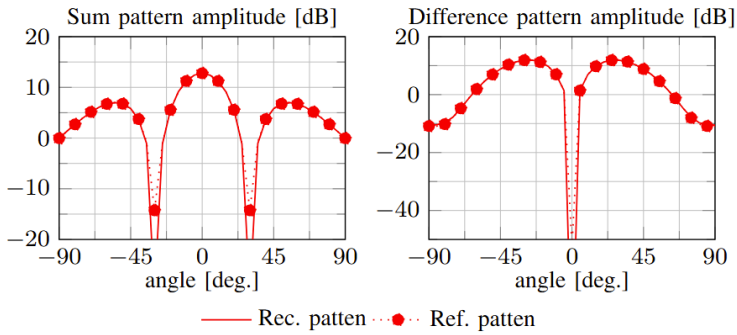

Figure 2.9: Recovered combined array patterns for sum and difference excitations.

The reconstructed sum and difference patterns (Fig. 2.9) exhibit relative errors below 0.6% and 0.8%, respectively, with deviations concentrated near deep nulls.

These results confirm that the proposed backscattering-based method enables accurate recovery of both element-level and array-level radiation characteristics through over-the-air measurements without direct port access.

Application to a 28 GHz RIS unit cell

The proposed backscattering-based extraction framework was validated experimentally on a reconfigurable intelligent surface (RIS) unit cell operating in the 28 GHz band. In contrast to conventional antenna arrays, the RIS element does not provide a well-defined RF port that can be directly accessed and calibrated. Instead, reconfiguration is achieved through tunable components embedded into the radiating aperture, which makes OTA-based characterization particularly attractive.

Figure 2.10 shows the fabricated unit cell, implemented as an end-folded patch loaded with a PIN diode and a varactor diode. Both the PIN diode and varactor enables continuous tuning through bias control. To study coupling effects, two unit cells were placed side-by-side, forming a 1×2 prototype with four tuning ports in total (two per unit cell). The monostatic measurement configuration is shown in Fig. 2.11a, where a chamber antenna is connected to a one-port VNA and used to illuminate the DUT and measure the backscat-

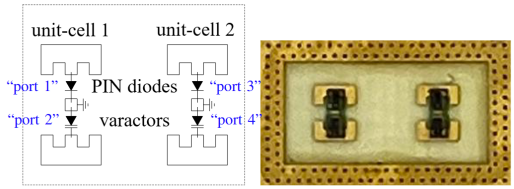

(a) DUT top layer drawing. (b) DUT top layer photo.

Figure 2.10: Unit-cell photo and drawing.

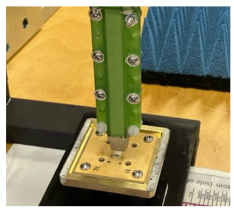

(a) Photo of the measurement setup.

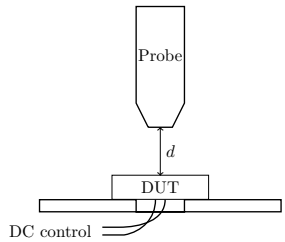

(b) Schematic drawing of the measurement setup.

Figure 2.11: Measurement setup for the RIS unit cell.

tered signal $\widehat{S}_{11}$ for different bias configurations.

The extraction requires a set of distinct load states. In practice, these states are realized by biasing the PIN and varactor diodes such that the corresponding reflection coefficients at the tuning ports are sufficiently separated. For this purpose, the diodes were separately measured and a nonlinear equivalent circuit model was fitted to the data, which was used during the measurement. Figure 2.12a shows the measured reflection coefficients at the PIN-diode and varactor-diode junctions over frequency, while Fig. 2.12b shows the measured coupling between the two tuning ports within a unit cell.

For each selected combination of diode bias states (i.e., a specific diagonal $\mathbf{\Gamma}$), the probe reflection coefficient $\widehat{S}_{11}$ was measured and the corresponding equivalent multiport scattering parameters were recovered using the procedure in Sec. 2.1 (Steps 1–3). The extracted scattering parameters were then converted to impedance parameters.

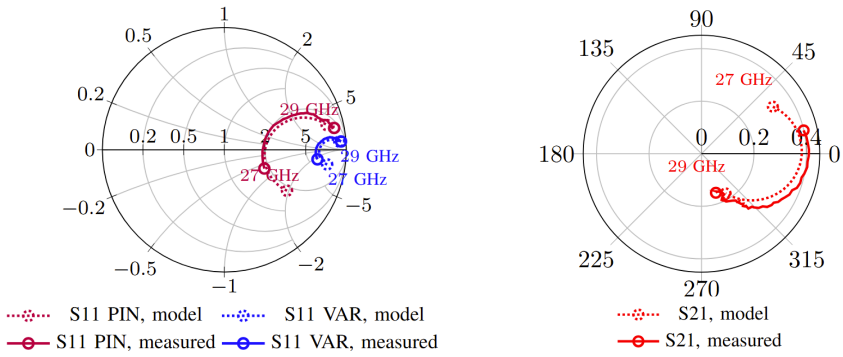

(a) Measured reflection coefficient at the PIN-diode and varactor-diode junctions.

(b) Measured coupling between varactor and PIN diode.

Figure 2.12: Measured S-parameters of the RIS tuning network.

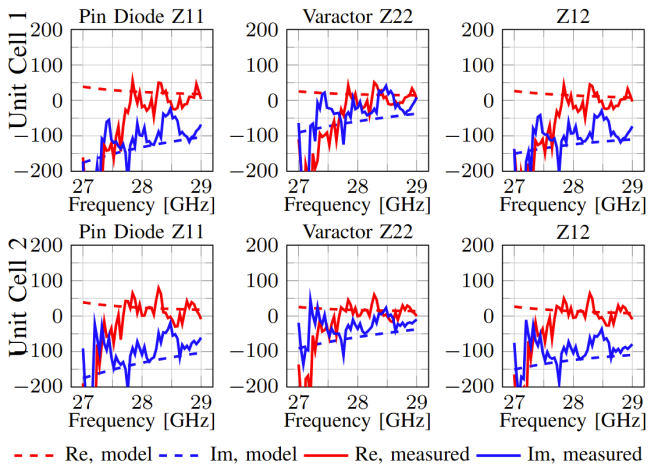

Figure 2.13: Extracted impedance parameters of the RIS tuning network (from reconstructed S-parameters).

Figure 2.13 shows the extracted impedance parameters, demonstrating that the proposed backscattering inversion can recover not only the effective port reflection behavior but also the mutual coupling between the tuning ports.

Overall, this experiment confirms that the proposed method can be applied to highly integrated RIS elements with embedded tunable components, enabling OTA validation in the 28 GHz band without direct RF access to unit-cell ports.

In summary, the proposed backscattering-based OTA framework enables extraction of the passive multiport scattering parameters of integrated antenna arrays without direct RF access to the antenna ports. Through controlled load modulation, phase correction post-processing step, and impedance renormalization, the passive S-parameter matrix of the antenna array is reconstructed. This method, in principle, can be used with already present RF front-end and do not necessarily entails complications in the antenna design. The method further supports embedded element pattern recovery and beamforming analysis, and its validity is confirmed through various simulations and measurements on a 28 GHz RIS unit cell.

CHAPTER 3

Active Device Characterization by Open-Loop Active Load-Pull

This chapter summarizes a self-contained open-loop active load-pull measurement system implemented on a single ZCU216 RFSoC evaluation board [47]. The setup utilizes two DACs and four high-speed ADCs of the RFSoC to simultaneously synthesize a programmable load impedance presented to the DUT and to sample the signals at its input and output terminals.

This architecture eliminates the need for external RF instrumentation such as signal generators and vector network analyzers. Combined with a compact in situ calibration model for load impedance synthesis, the approach provides an accurate, repeatable, and cost-effective platform for active device characterization under controlled impedance conditions.

Measurement setup and operating principle

The proposed system is built around the ZCU216 RFSoC evaluation board, which provides integrated high-speed DACs and ADCs for stimulus generation and waveform acquisition. Signal generation uses direct digital synthesis (DDS) at 8 GSPS (second Nyquist zone), while receive part uses undersam-

pling at 2.5 GSPS. Out-of-band images are suppressed using bandpass filters (4.9–6.2 GHz).

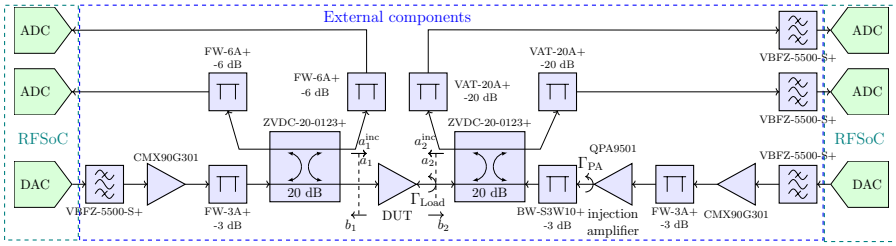

Figure 3.1: System-level schematic of the RFSoC-based open-loop active load-pull setup.

A practical implementation of the RF path includes directional couplers, attenuators, an injection amplifier, and a receive preamplifier.

The key idea is to synthesize a desired load reflection coefficient Γ_{Load} at the DUT output plane by controlling the ratio of two DAC-generated incident waves and compensating for unknown reflections and phase shifts in the measurement path through an in situ calibration model.

In situ calibration model for load synthesis

In active load-pull, mismatch between the DUT and the injection amplifier leads to multiple reflections, while unknown cable length and nonlinear behavior distort the amplitude and phase of the synthesized waves. These effects prevent direct control of Γ_{Load} using only the programmed DAC waveforms.

To address this, a simple calibration model is introduced by describing the total incoming and outgoing waves at the DUT output plane (a_2, b_2) as a geometric series. For a linearized case,

$$a_2 = \frac{a_2^{\text{inc}} + a_1^{\text{inc}} S_{21}^{\text{DUT}} \Gamma_{\text{PA}} \alpha^2 e^{-j2\Delta\phi}}{1 - S_{22}^{\text{DUT}} \Gamma_{\text{PA}} \alpha^2 e^{-j2\Delta\phi}}, \tag{3.1a}$$

$$b_2 = \frac{a_2^{\text{inc}} S_{22}^{\text{DUT}} + a_1^{\text{inc}} S_{21}^{\text{DUT}}}{1 - S_{22}^{\text{DUT}} \Gamma_{\text{PA}} \alpha^2 e^{-j2\Delta\phi}}, \tag{3.1b}$$

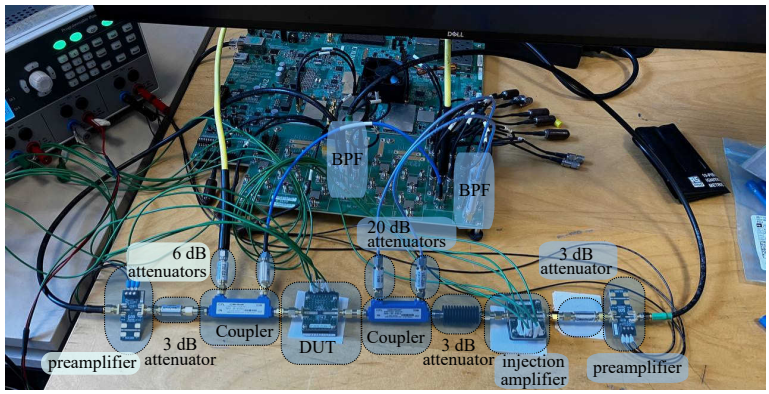

Figure 3.2: Photo of the implemented load-pull measurement setup.

where a_i^{inc} denote the incident waves synthesized by the DACs, Γ_{PA} is the reflection coefficient of the injection amplifier, and $\alpha e^{-j\Delta\phi}$ models the one-way attenuation and phase shift from the DUT plane to the injection amplifier.

The effective reflection coefficient seen by the DUT is then

$$\Gamma_{\text{Load}} = \frac{a_2}{b_2}. \tag{3.2}$$

Defining the programmed reflection coefficient as

$$\Gamma_{\text{set}} = \frac{a_2^{\text{inc}}}{a_1^{\text{inc}}}, \tag{3.3}$$

the model can be expressed in the compact rational form

$$\Gamma_{\text{Load}} = \frac{\alpha_0 + \alpha_1 \Gamma_{\text{set}}}{1 + \alpha_2 \Gamma_{\text{set}}}, \tag{3.4}$$

where $\{\alpha_n\}$ capture the combined effect of unknown reflections, attenuation, and phase shifts in the signal path. Since the DUT behavior is power-dependent, the model parameters are fitted separately for each input power level.

Calibration and synthesis accuracy

The model parameters are obtained by nonlinear least-squares fitting (e.g., `lsqnonlin`) initialized from three calibration points distributed over the Smith

chart, for example $\Gamma_{\text{set}} \in \{0, 0.5, 0.5j\}$. After calibration, the synthesized reflection coefficients closely match their goals (Fig. 3.3).

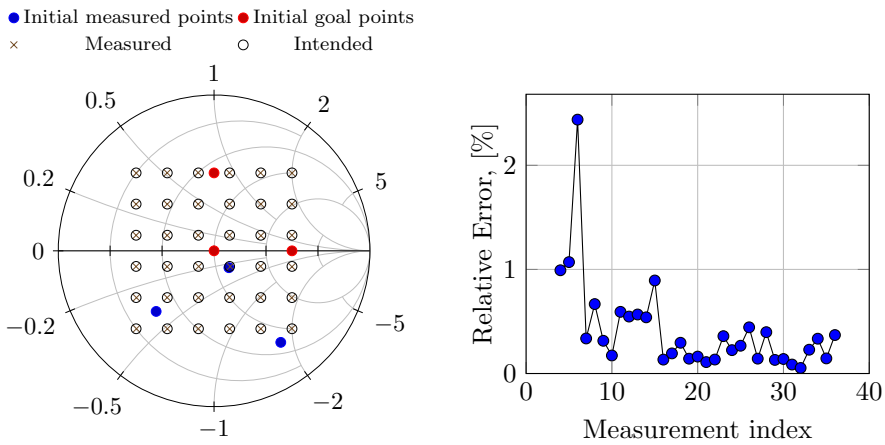

(a) Synthesized Γ_{Load}.

(b) Relative error in reflection coefficient synthesis.

Figure 3.3: Model accuracy and comparison to measured data.

The error metrics are defined as

$$\text{Relative error} = \frac{|\Gamma_{\text{measured}} - \Gamma_{\text{goal}}|}{|\Gamma_{\text{goal}}|} \times 100\%,$$

$$\text{Absolute error} = |\Gamma_{\text{measured}} - \Gamma_{\text{goal}}|.$$

Measured results show sub-2.5% relative error and below 0.5% on average (excluding the chart center), with absolute error below approximately 0.03 Ohm over the Smith chart.

Example measurements

The setup was demonstrated in two regimes: (i) operation as a compact two-port VNA for small-signal measurements, and (ii) active load-pull measurements of a commercial RF power amplifier.

A 3D-printed horn antenna was measured and compared against a laboratory VNA, showing deviations below approximately 0.5 dB, mainly attributed to environmental standing waves.

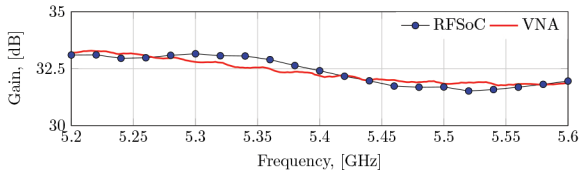

Figure 3.6: Small-signal gain of the power amplifier: RFSoC versus reference VNA.

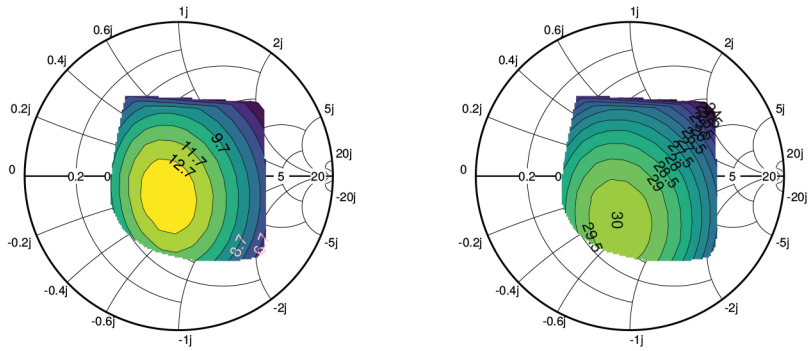

(a) PAE contour plot.

(b) P_{out} contour plot.

Figure 3.7: Load-pull contour plots: (a) PAE and (b) output power.

model enables accurate load synthesis without prior DUT characterization, and experimental results demonstrate strong agreement with conventional instrumentation while substantially reducing system complexity and measurement cost.

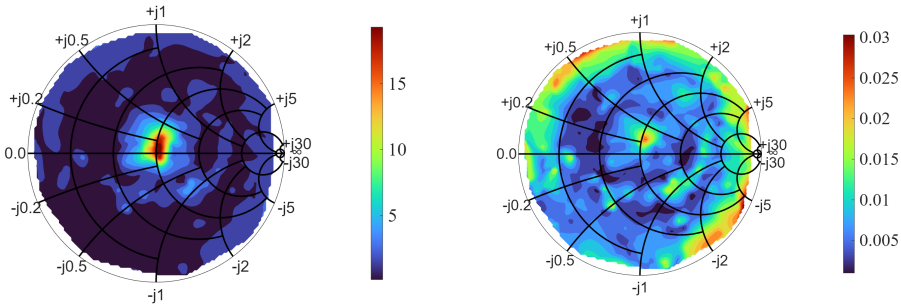

(a) Relative error, [%]. **(b)** Absolute error.

Figure 3.4: Measured error depending on the position on the Smith chart.

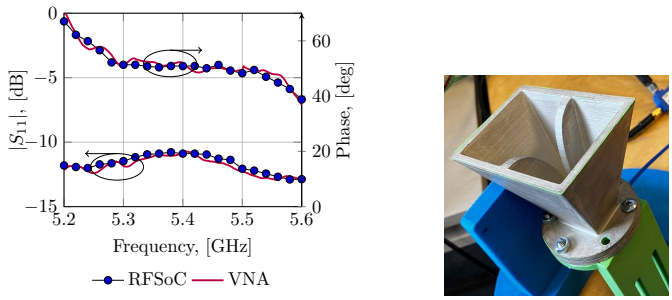

(a) S_{11} magnitude and phase. **(b)** Photo of the horn.

Figure 3.5: Horn antenna return loss: RFSoC measurement versus reference VNA.

The small-signal gain of the QPA9501 power amplifier was measured and matched the reference VNA and datasheet trends, with a peak deviation of approximately 0.5 dB.

Finally, load-pull measurements were performed at 5.4 GHz. The measured contours for power-added efficiency (PAE) and output power identify different optimal impedances: the highest PAE occurs near $41.7 - j13.2\ \Omega$, while the maximum output power occurs near $32.2 - j11.3\ \Omega$. This separation is expected under overdriven conditions, where efficiency- and power-optimal terminations shift away from 50 Ω.

In summary, the presented RFSoC-based open-loop active load-pull approach provides a compact and cost-effective platform for characterizing active RF devices under controlled impedance environments. The in situ calibration

CHAPTER 4

Summary of included papers

This chapter provides a summary of the included papers.

4.1 Paper A

Iaroslav Shilinkov, Rob Maaskant
Antenna Array Measurements by a Scalable Backscatter Modulation Procedure
IEEE Antennas and Wireless Propagation Letters,
vol. 23, no. 10, pp. 2989-2993, Oct. 2024.
 DOI 10.1109/LAWP.2024.3417335 .

This paper introduces a scalable over-the-air backscatter modulation technique for systematic characterization of antenna arrays. A generic matrix-based formulation enables extraction of full passive S-parameters, embedded element patterns, and array radiation characteristics using only three switchable load terminations per element. A renormalization procedure is incorporated to simplify practical implementation at mm-wave frequencies, and the sign ambiguity in phase retrieval of coupling coefficients is resolved. Numer-

ical validation for four- and eight-element dipole arrays demonstrates highly accurate recovery of impedance and radiation properties.

IS developed the theoretical framework, implemented the recovery algorithms, performed simulations, and wrote the manuscript. RM supervised the research, contributed to conceptual development, and reviewed and refined the manuscript.

4.2 Paper B

Iaroslav Shilinkov, Rob Maaskant, Gregor Lasser
Open-loop Active Load-pull Setup Using the ZCU216 Radio Frequency System-on-Chip
IEEE Microwave and Wireless Technology Letters,
vol. 35, no. 12, pp. 2121-2124, Dec. 2025.
 DOI 10.1109/LMWT.2025.3633956.
.

This paper presents a fully self-contained active open-loop load-pull measurement system implemented on a commercial RFSoC evaluation board. By leveraging integrated high-speed DACs and ADCs, the setup eliminates the need for external signal generators and vector network analyzers. A simple calibration and impedance synthesis method is introduced to accurately realize arbitrary load impedances without prior knowledge of the device under test. The system is experimentally validated through antenna return-loss measurements, small-signal gain characterization, and active load-pull measurements of a commercial RF power amplifier at 5.4 GHz.

IS conceived the system architecture, developed the calibration and impedance synthesis algorithms, implemented the measurement software, carried out experiments, and wrote the manuscript. RM and GL contributed to conceptual discussions, supervision, interpretation of results, and manuscript refinement.

4.3 Paper C

Iaroslav Shilinkov, Viktor Chernikov, Rob Maaskant, Marianna Ivashina
Antenna Characterization by the Back-Scattering Measurement Method Using the Integrated RF-Frontend as Load Modulation Device

25th International Conference on Electromagnetics in Advanced Applications (ICEAA), 2024.
 DOI 10.1109/ICEAA61917.2024.10701632 .

This paper demonstrates an over-the-air back-scattering measurement technique for characterizing antennas integrated with RF frontends. Instead of employing dedicated load-switching circuitry, the operational states of existing frontend components such as power amplifiers, low-noise amplifiers, and Tx/Rx switches are used to modulate the antenna load impedance. The method enables recovery of the antenna reflection coefficient and realized gain without physical port access. Numerical validation at 100 GHz using on-chip antennas and two frontend architectures confirms highly accurate parameter extraction and analyzes sensitivity to measurement noise and antenna separation.

IS developed the theoretical formulation, implemented the numerical validation, performed simulations, and prepared the manuscript. VC contributed to circuit modeling and frontend implementation. RM and MI supervised the research, contributed to conceptual development, and reviewed the manuscript.

4.4 Paper D

Iaroslav Shilinkov, Oleg Iupikov, Pavlo Krasov, Yuqing Zhu, Rob Maaskant, Marianna Ivashina
Measurement of Reconfigurable Intelligent Surfaces Through the Back-Scattering Method: Demonstration at 28 GHz
19th European Conference on Antennas and Propagation (EuCAP),Stockholm, Sweden, 2025.
 DOI 10.23919/EuCAP63536.2025.10999375 .

This paper presents an over-the-air back-scattering measurement technique for characterizing reconfigurable intelligent surface (RIS) unit cells without direct RF port access. The method enables recovery of the input impedance and coupling characteristics of RIS unit cells by exploiting electronically tunable diode loads to modulate the backscattered field. Experimental validation at 28 GHz is performed on a two-unit-cell RIS prototype featuring independently controlled PIN and varactor diodes. The results demonstrate practical feasibility of impedance extraction and highlight the influence of diode mod-

eling accuracy and measurement noise on parameter recovery.

IS developed the measurement framework, implemented the parameter extraction procedure, conducted experiments, and prepared the manuscript. OI, PK, and YZ contributed to RIS prototype design, diode modeling, and measurements. RM and MI supervised the research, contributed to conceptual development, and reviewed the manuscript.

CHAPTER 5

Concluding Remarks and Future Work

5.1 Concluding remarks

This thesis investigated the problem of AiA measurements. Conceptually this problem splits into two:

1. Reconstruction of passive multiport antenna parameters without direct port access.
2. Large-signal device characterization.

In Chapter 2, a backscattering-based method was formulated to recover the passive S-parameters of multi-element antenna arrays from over-the-air measurements with controllable load terminations. A scalable matrix formulation was introduced, allowing systematic extraction of S-parameters. The analysis explicitly addressed phase-sign ambiguity in the recovered transmission coefficients and introduced an impedance renormalization procedure suitable for practical mm-wave measurements. Numerical studies demonstrated accurate reconstruction for four- and eight-element arrays.

The approach was further illustrated for a 28 GHz reconfigurable intelligent surface unit cell containing tunable components embedded in aperture. The

results showed that impedance-related parameters can, in principle, be reconstructed through load modulation, although the accuracy depends strongly on load modeling, tuning range, and measurement dynamic range.

In Chapter 3, a fully self-contained open-loop active load-pull system based on a commercial RFSoC evaluation board was presented. The setup removes the need for external RF generators and VNAs by using integrated DACs and ADCs. A simple in situ calibration model was introduced to compensate for multiple reflections and unknown phase shifts in the measurement path. Experimental results demonstrated accurate return-loss measurements, small-signal gain validation, and large-signal load-pull contours at 5.4 GHz.

The work therefore contributes:

- A scalable passive parameter reconstruction framework for antenna arrays using backscattering load modulation with practical demonstration applied to RIS.
- A compact and reconfigurable implementation of open-loop active load-pull.

5.2 Future work

The next natural step is the design and validation of active integrated antenna (AIA) arrays. This requires consistent co-simulation of nonlinear power amplifiers and multi-element antenna arrays using either modeled or measured array parameters.

The passive multiport reconstruction framework developed in this thesis provides a mechanism to extract array S-parameters even when direct port access is unavailable. In future work, these reconstructed passive models can be embedded into nonlinear circuit simulations to evaluate their adequacy for AIA co-design.

Furthermore, the RFSoC-based active load-pull platform enables programmable impedance synthesis at the device plane. This capability can be used to emulate impedance trajectories representative of array-induced loading under beam steering and mutual coupling. By combining array-derived active reflection coefficients with programmable load synthesis, the impact of realistic array environments on PA efficiency, linearity, and stability can be studied experimentally.

Overall, the presented work provides two complementary building blocks: passive multiport reconstruction without direct port access and programmable impedance synthesis using compact hardware. Future research will explore how these tools can be integrated into a consistent co-design and validation workflow for active integrated antenna arrays.

References

[1] S. H. Han and J. H. Lee, "An overview of peak-to-average power ratio reduction techniques for multicarrier transmission," *IEEE Wireless Communications*, vol. 12, no. 2, pp. 56–65, 2005.

[2] S. C. Cripps, *RF Power Amplifiers for Wireless Communications*, 2nd. Artech House, 2006.

[3] E. Björnson, J. Hoydis, and L. Sanguinetti, "Massive mimo networks: Spectral, energy, and hardware efficiency," *Foundations and Trends in Signal Processing*, vol. 11, no. 3–4, pp. 154–655, 2017.

[4] C. Freitag, M. Berners-Lee, K. Widdicks, B. Knowles, G. Blair, and A. Friday, "The climate impact of ict: A review of estimates, trends and regulations," *arXiv preprint arXiv:2102.02622*, 2021.

[5] J. Lorincz, A. Capone, and J. Wu, "Greener, energy-efficient and sustainable networks: State-of-the-art and new trends," *Sensors*, vol. 19, no. 22, p. 4864, 2019.

[6] European Parliament and of the Council, *Regulation (eu) 2021/1119 establishing the framework for achieving climate neutrality (european climate law)*, CELEX: 32021R1119, Official Journal of the European Union, L 243, pp. 1–17, Jun. 30, 2021.

[7] M. V. Ivashina, "Joint design and co-integration of antenna-ic systems," in *2019 13th European Conference on Antennas and Propagation (EuCAP)*, 2019, pp. 1–7.

[8] M. de Kok, S. Monni, M. van Heijningen, A. Garufo, A. B. Smolders, and U. Johannsen, "A review of pa-antenna co-design: Direct matching, harmonic tuning and power combining," in *2022 52nd European Microwave Conference (EuMC)*, 2022, pp. 536–539.

[9] S. Shahramian, M. J. Holyoak, A. Singh, and Y. Baeyens, "A fully integrated 384-element, 16-tile, W -band phased array with self-alignment and self-test," *IEEE Journal of Solid-State Circuits*, vol. 54, no. 9, pp. 2419–2434, 2019.

[10] Y. Wang, A. Hong, J. Lai, *et al.*, "D/j-band on-chip dual-band antenna for low-cost fully integrated terahertz radar," *IEEE Antennas and Wireless Propagation Letters*, vol. 24, no. 12, pp. 4555–4559, 2025.

[11] M. SalarRahimi, E. Vilela Pinto dos Anjos, P. Taghikhani, *et al.*, "A cost-efficient 28 ghz integrated antenna array with full impedance matrix characterization for 5g nr," *IEEE Antennas and Wireless Propagation Letters*, vol. 19, no. 4, pp. 666–670, 2020.

[12] X. Gu, D. Liu, Y. Suto, *et al.*, "Novel phased array antenna-in-package development and active module demonstration for 5g millimeter-wave wireless communication," in *2021 IEEE 71st Electronic Components and Technology Conference (ECTC)*, 2021, pp. 1144–1149.

[13] Y. Zhang and J. Mao, "An overview of the development of antenna-in-package technology for highly integrated wireless devices," *Proceedings of the IEEE*, vol. 107, no. 11, pp. 2265–2280, 2019.

[14] Y. Zhang, "Antenna-in-package (aip) technology," *Engineering*, vol. 11, pp. 18–20, 2022, ISSN: 2095-8099.

[15] D. G. Kam, D. Liu, A. Natarajan, S. Reynolds, and B. A. Floyd, "Low-cost antenna-in-package solutions for 60-ghz phased-array systems," in *19th Topical Meeting on Electrical Performance of Electronic Packaging and Systems*, 2010, pp. 93–96.

[16] W. Hong, K.-H. Baek, and A. Goudelev, "Multilayer antenna package for ieee 802.11ad employing ultralow-cost fr4," *IEEE Transactions on Antennas and Propagation*, vol. 60, no. 12, pp. 5932–5938, 2012.

[17] W. Hong, K.-h. Baek, and A. Goudelev, "Grid assembly-free 60-ghz antenna module embedded in fr-4 transceiver carrier board," *IEEE Transactions on Antennas and Propagation*, vol. 61, no. 4, pp. 1573–1580, 2013.

[18] E. Cohen, M. Ruberto, M. Cohen, O. Degani, S. Ravid, and D. Ritter, "A cmos bidirectional 32-element phased-array transceiver at 60 ghz with ltcc antenna," *IEEE Transactions on Microwave Theory and Techniques*, vol. 61, no. 3, pp. 1359–1375, 2013.

[19] M. Alibakhshikenari, E. M. Ali, M. Soruri, *et al.*, "A comprehensive survey on antennas on-chip based on metamaterial, metasurface, and substrate integrated waveguide principles for millimeter-waves and terahertz integrated circuits and systems," *IEEE Access*, vol. 10, pp. 3668–3692, 2022.

[20] F. Gutierrez, S. Agarwal, K. Parrish, and T. S. Rappaport, "On-chip integrated antenna structures in cmos for 60 ghz wpan systems," *IEEE Journal on Selected Areas in Communications*, vol. 27, no. 8, pp. 1367–1378, 2009.

[21] W.-C. Liao, R. Maaskant, T. Emanuelsson, V. Vassilev, O. Iupikov, and M. Ivashina, "A directly matched pa-integrated K-band antenna for efficient mm-wave high-power generation," *IEEE Antennas and Wireless Propagation Letters*, vol. 18, no. 11, pp. 2389–2393, 2019.

[22] W.-L. Liu, J.-D. Zhou, J.-Y. Deng, *et al.*, "Class-F^{-1} asymmetric doherty power amplifier integrated slot antenna array with high efficiency and large back-off range," *IEEE Transactions on Microwave Theory and Techniques*, vol. 73, no. 11, pp. 8879–8892, 2025.

[23] M. S. Sharawi, S. K. Dhar, O. Hammi, and F. M. Ghannouchi, "Miniaturised active integrated antennas: A co-design approach," *IET Microwaves, Antennas & Propagation*, vol. 10, no. 8, pp. 871–879, 2016.

[24] S. Li, T. Chi, and H. Wang, "Multi-feed antenna and electronics codesign: An e-band antenna-lna front end with on-antenna noise-canceling and G_m-boosting," *IEEE Journal of Solid-State Circuits*, vol. 55, no. 12, pp. 3362–3375, 2020.

[25] F. Urbani, F. Bilotti, A. Alù, and L. Vegni, "Vco active integrated antenna with reactive impedance surfaces," *Microwave and Optical Technology Letters*, vol. 47, no. 1, pp. 82–86, 2005.

[26] A. Ferrero, F. Sanpietro, U. Pisani, and C. Beccari, "Novel hardware and software solutions for a complete linear and nonlinear microwave device characterization," *IEEE Transactions on Instrumentation and Measurement*, vol. 43, no. 2, pp. 299–305, 1994.

[27] F. Blache, J. Nebus, P. Bouysse, and J. Villotte, "A novel computerized multiharmonic active load-pull system for the optimization of high efficiency operating classes in power transistors," in *Proceedings of 1995 IEEE MTT-S International Microwave Symposium*, 1995, 1037–1040 vol.3.

[28] J. A. Reynoso-Hernández, M. A. Pulido-Gaytan, T. Niubó-Alemán, and M. Molina-Ceseña, "Advances in microwave large-signal metrology: From vector-receiver load-pull to vector signal network analyzer and time-domain load-pull implementations (invited paper)," *Electronics*, vol. 11, no. 7, 2022, ISSN: 2079-9292.

[29] S. Bensmida, E. Bergeault, G. Abib, and B. Huyart, "Power amplifier characterization: An active load-pull system based on six-port reflectometer using complex modulated carrier," *IEEE Transactions on Microwave Theory and Techniques*, vol. 54, no. 6, pp. 2707–2712, 2006.

[30] M. S. Hashmi, A. L. Clarke, S. P. Woodington, J. Lees, J. Benedikt, and P. J. Tasker, "An accurate calibrate-able multiharmonic active load–pull system based on the envelope load–pull concept," *IEEE Transactions on Microwave Theory and Techniques*, vol. 58, no. 3, pp. 656–664, 2010.

[31] M. Thorsell and K. Andersson, "Fast multiharmonic active load–pull system with waveform measurement capabilities," *IEEE Transactions on Microwave Theory and Techniques*, vol. 60, no. 1, pp. 149–157, 2012.

[32] M. Marchetti, M. J. Pelk, K. Buisman, W. C. E. Neo, M. Spirito, and L. C. N. de Vreede, "Active harmonic load–pull with realistic wideband communications signals," *IEEE Transactions on Microwave Theory and Techniques*, vol. 56, no. 12, pp. 2979–2988, 2008.

[33] A. M. Angelotti, G. P. Gibiino, T. S. Nielsen, D. Schreurs, and A. Santarelli, "Wideband active load–pull by device output match compensation using a vector network analyzer," *IEEE Transactions on Microwave Theory and Techniques*, vol. 69, no. 1, pp. 874–886, 2021.

[34] M. Spirito, M. J. Pelk, F. van Rijs, S. J. C. H. Theeuwen, D. Hartskeerl, and L. C. N. de Vreede, "Active harmonic load–pull for on-wafer out-of-band device linearity optimization," *IEEE Transactions on Microwave Theory and Techniques*, vol. 54, no. 12, pp. 4225–4236, 2006.

[35] J. Benedikt, R. Gaddi, P. Tasker, M. Goss, and M. Zadeh, "High power time domain measurement system with active harmonic load-pull for high efficiency base station amplifier design," in *2000 IEEE MTT-S International Microwave Symposium Digest (Cat. No.00CH37017)*, vol. 3, 2000, 1459–1462 vol.3.

[36] R. Argaez-Ramirez, J.-R. Perez-Cisneros, and C. Fager, "Investigation of power amplifier performance under load mismatch conditions," in *2021 IEEE Topical Conference on RF/Microwave Power Amplifiers for Radio and Wireless Applications (PAWR)*, 2021, pp. 41–43.

[37] D. Nopchinda and K. Buisman, "Measurement technique to emulate signal coupling between power amplifiers," *IEEE Transactions on Microwave Theory and Techniques*, vol. 66, no. 4, pp. 2034–2046, 2018.

[38] I. R. R. Barani, L. A. Bronckers, and A. C. Reniers, "Integrated-antenna over-the-air testing for millimeter-wave applications: An overview of systems and uncertainty [measurements corner]," *IEEE Antennas and Propagation Magazine*, vol. 64, no. 5, pp. 97–110, 2022.

[39] K. Rasilainen, M. E. Leinonen, M. J. Nokandi, *et al.*, "Ota measurement technique for sub-thz integrated lens antennas," in *2023 100th ARFTG Microwave Measurement Conference (ARFTG)*, 2023, pp. 1–4.

[40] X. An, Y. Wang, Q. Zhang, W. Wang, and Y. Liu, "An efficient multi-probe enabled midfield over-the-air test method for 5g base station antenna pattern reconstruction," *Electronics Letters*, vol. 60, no. 19, e13303, 2024.

[41] E. Oblitas, J. L. Salazar-Cerreno, A. Bonthron, E. Megerdichian, and M. Achour, "Enhancing antenna in package array calibration: A hybrid multi-axis scanner enabling near-field and far-field measurements for over-the-air calibration," in *2023 Antenna Measurement Techniques Association Symposium (AMTA)*, 2023, pp. 1–6.

[42] R. Heijs, T. Stek, T. van den Biggelaar, R. Budé, and A. Hubrechsen, "Over-the-air noise-figure measurements of active integrated antennas at w-band," in *2024 18th European Conference on Antennas and Propagation (EuCAP)*, 2024, pp. 1–4.

[43] A. J. van den Biggelaar, S. J. Geluk, B. F. Jamroz, *et al.*, "Accurate gain measurement technique for limited antenna separations," *IEEE Transactions on Antennas and Propagation*, vol. 69, no. 10, pp. 6772–6782, 2021.

[44] A. van den Biggelaar, D. Daverveld, A. Reniers, A. Smolders, and U. Johannsen, "Determining the input reflection coefficient of integrated antennas using over-the-air measurements under near-field conditions," *International Journal of Microwave and Wireless Technologies*, vol. 13, no. 4, pp. 390–396, 2021.

[45] D. Kruglov, P. Krasov, O. Iupikov, A. Vilenskiy, M. Ivashina, and R. Maaskant, "Contactless measurement of a D-band on-chip antenna using an integrated reflective load switch," *IEEE Antennas and Wireless Propagation Letters*, 2023.

[46] K. Kurokawa, "Power waves and the scattering matrix," *IEEE Transactions on Microwave Theory and Techniques*, vol. 13, no. 2, pp. 194–202, 1965.

[47] AMD. "Zynq ultrascale+ rfsoc." (2024), [Online]. Available: `https://www.amd.com/en/products/adaptive-socs-and-fpgas/soc/zynq-ultrascale-plus-rfsoc.html` (visited on 03/11/2026).